

Tonga eruption triggered waves propagating globally from surface to edge of space

Corwin J Wright^{*1}, Neil P Hindley¹, M Joan Alexander², Mathew Barlow³, Lars Hoffmann⁴, Cathryn N Mitchell¹, Fred Prata^{5,6}, Marie Bouillon⁷, Justin Carstens⁸, Cathy Clerbaux⁷, Scott M Osprey⁹, Nick Powell¹⁰, Cora E Randall^{11,12}, and Jia Yue^{13,14}

1. Centre for Space, Atmospheric and Oceanic Science, University of Bath, Bath, UK
 2. Northwest Research Associates, Boulder, Colorado, USA
 3. Environmental, Earth & Atmospheric Sciences, University of Massachusetts Lowell, Massachusetts, USA
 4. Jülich Supercomputing Center, Forschungszentrum Jülich, Jülich, Germany
 5. AIRES, Mt Eliza, Victoria, Australia
 6. School of Electrical Engineering, Computing & Mathematical Science, Curtin University, Western Australia
 7. LATMOS/IPSL, Sorbonne Université/UVSQ/CNRS, Paris, France
 8. Center for Space Science and Engineering Research, Bradley Department of Electrical and Computer Engineering, Virginia Tech, Blacksburg, VA, USA
 9. Atmospheric, Oceanic and Planetary Physics, Department of Physics, University of Oxford, Oxford, UK
 10. Raytheon Technologies
 11. Laboratory for Atmospheric and Space Physics, University of Colorado Boulder, Boulder, CO, USA
 12. Department of Atmospheric and Oceanic Sciences, University of Colorado Boulder, Boulder, CO, USA
 13. NASA Goddard Space Flight Center, Community Coordinated Modeling Center, Greenbelt, MD, USA
 14. Physics Department, Catholic University of America, Washington, DC, USA
- * Corresponding author, c.wright@bath.ac.uk

Abstract

The January 2022 Hunga Tonga–Hunga Ha‘apai eruption was one of the most explosive volcanic events observed in the modern era^{1,2}, producing a vertical plume which peaked more than 50km above the Earth. The initial explosion and subsequent plume triggered atmospheric waves which propagated around the world multiple times. Here, we combine a comprehensive set of satellite and ground-based observations to analyse and quantify this wave response, from surface to ionosphere. A broad spectrum of waves was triggered by the initial explosion, including Lamb waves^{3,4} propagating at 318.2 ± 6 ms^{-1} at surface level and between 308 ± 5 to 319 ± 4 ms^{-1} in the stratosphere, and fast gravity waves⁵ propagating at 238 ± 3 to 269 ± 3 ms^{-1} in the stratosphere. Atmospheric gravity waves at sub-ionospheric heights have not previously been observed propagating either at this speed or over the whole Earth from a single identifiable source^{6,7}. Latent heat release from water and hot ash in the plume remained the most significant individual gravity wave source at any location for the next 12 hours, producing circular wavefronts visible across the Pacific basin in satellite gravity wave observations. A single source dominating such a large region is also unique in the observational record. The Hunga Tonga eruption represents a key natural experiment in how the atmosphere responds to a sudden point-source-driven state change, which will be of significant use for improving atmospheric weather and climate models.

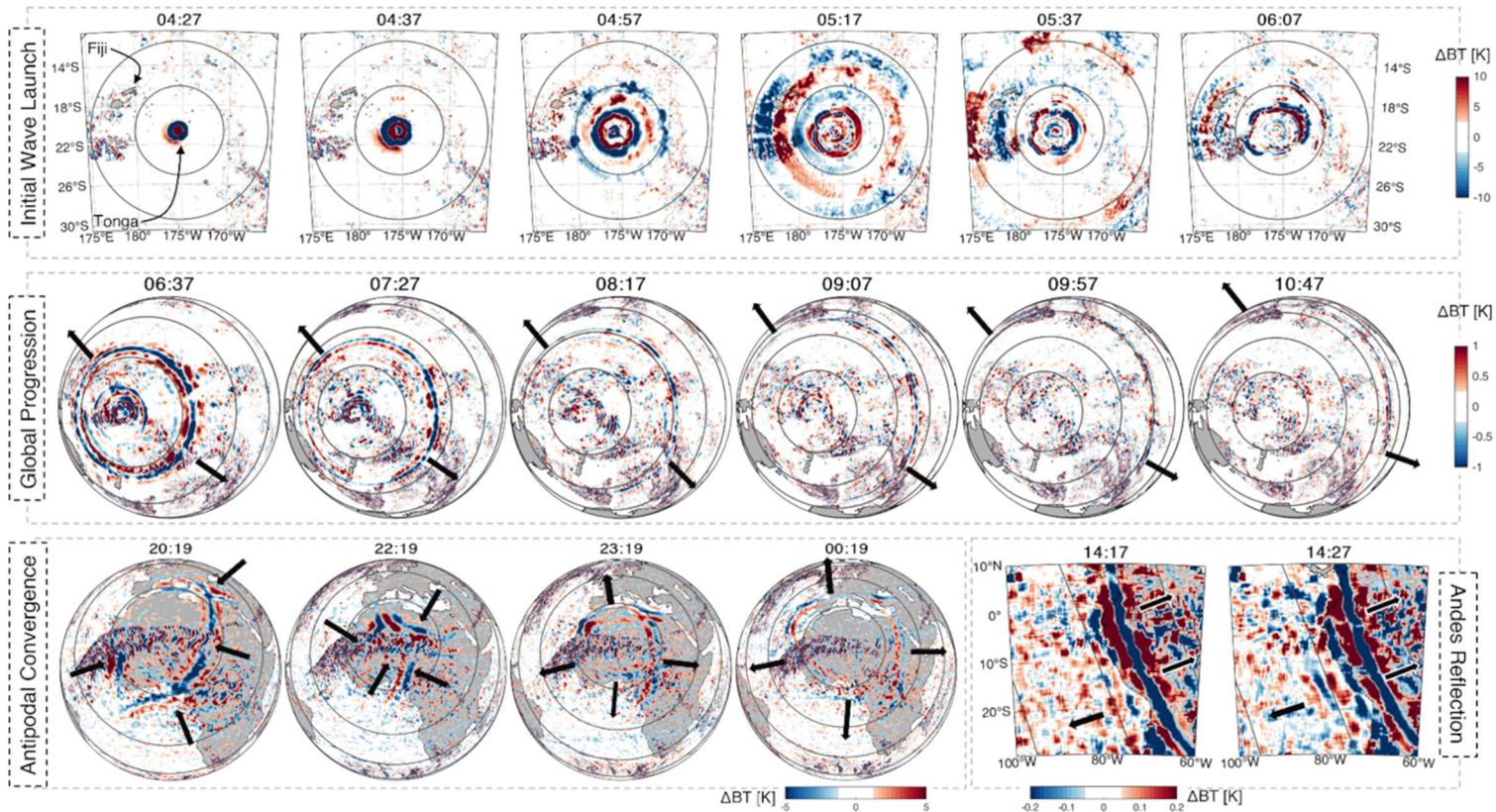
On the 15th of January 2022, the Hunga Tonga–Hunga Ha‘apai submarine volcano (20.54°S , 175.38°W , hereafter ‘Hunga Tonga’) erupted, producing a vertical plume >30 km tall with overshooting tops above 55 km, a record in the satellite era⁸ and likely longer². From surface-pressure data, we estimate a single-event energy release from the initial explosion of between 10-28 EJ, likely larger than the 1991 Mt Pinatubo eruption (~ 10 EJ²), and possibly comparable to Krakatoa in 1883 (~ 30 EJ²) (see Methods and Extended Data Figures 1a,b).

48 Large explosions such as volcanoes and nuclear tests are theoretically understood to produce
 49 atmospheric waves^{9,10} across a range of length and frequency scales. At horizontally-short
 50 wavelengths, these include external Lamb waves^{3,4,11}, acoustic waves¹⁰ and internal gravity
 51 waves¹². In addition to explosion-generated waves, volcanoes can also act as a sustained
 52 wave source after the initial eruption via updrafts and heating associated with plume
 53 convection^{13,14}.

54 In practice, observations of such waves at non-acoustic frequencies after volcanic eruptions
 55 are rare. Krakatoa⁴ and Pinatubo¹⁵, amongst others, produced strong Lamb waves visible in
 56 surface pressure. Internal waves in the boundary layer have been inferred from seismography,
 57 barometry and infrasound for eruptions including El Chichon¹³ (1982), Pinatubo¹³ and
 58 Okmok¹⁴ (2008). In the free atmosphere, local gravity wave activity associated with plume
 59 convection has been seen in mesospheric nightglow over the La Soufriere (2021) and
 60 Calbuco¹² (2015) eruptions and in local cloud over eruptions including Cumbre Vieja (2021).
 61 Re-examination of 1990s Advanced Very High Resolution Radiometer data also shows
 62 waves in cloud above Pinatubo (Extended Data Figure 2). Finally, an electron-density
 63 ionospheric wave response is usually observed^{16,17}, with the response magnitude proposed as
 64 a metric of volcano explosive power¹⁸.

65 There is however no direct observational evidence for long-distance propagation in the free
 66 neutral atmosphere of either Lamb or gravity waves triggered by volcanoes. Pre-2000s

Figure 1: Initial Lamb wave propagation in the troposphere: Brightness temperature changes observed by (top two rows) GOES, (bottom left) Meteosat Spinning Enhanced Visible and InfraRed Imager (SEVIRI) and (bottom right) GOES-EAST. Range rings indicate distance from Hunga Tonga in (top row) 500km and (lower rows) 2000km steps. To reduce noise from weather systems, global and antipodal panels have been processed with a 200km-radius Wiener filter, and Andes panels with a 400km boxcar and 72-km-radius Wiener filter. Black arrows indicate approximate wave location and propagation direction. All times UTC.



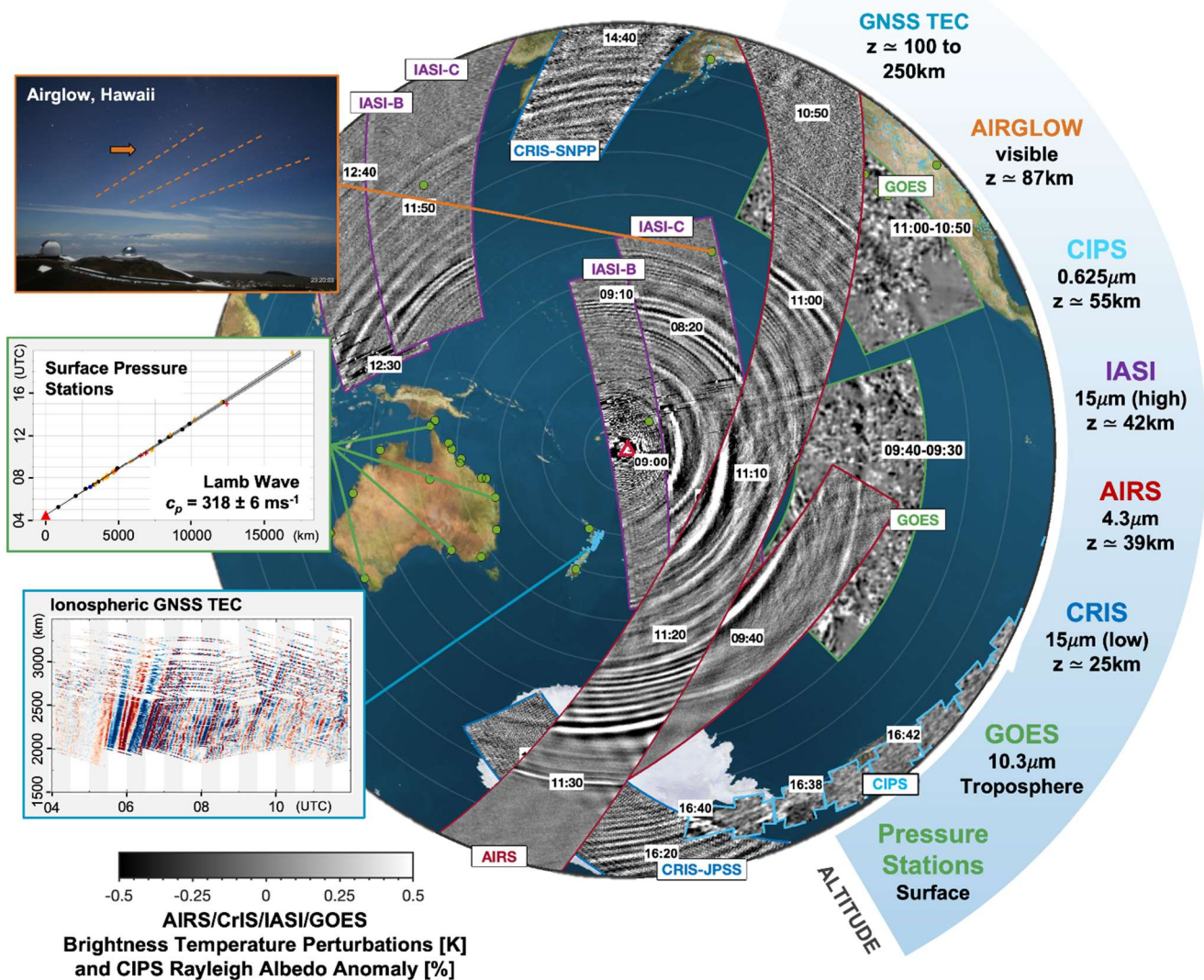


Figure 2: Initial gravity and Lamb wave propagation at all heights: Combined measurements of the initial wave release from multiple platforms, listed with their approximate altitudes at right and at times as indicated by overlaid text labels. Inset panels showing pressure (green outline) and TEC (blue outline) distance/time series are reproduced as Extended Data Figures 1d and 3 respectively. Note that AIRS, CrIS and IASI all measure the same three stratospheric altitude channels, but only one is used here from each instrument to show all levels while maintaining visual clarity; due to the long vertical wavelengths of the observed waves, all three levels are near-identical. Airglow inser shows a northward view containing the Lamb wavefront at 09:20 UTC, ~30 minutes after the wave passed overhead.

67 satellite observations had insufficient resolution and coverage to measure such waves, and no
 68 event since⁶ has produced a wave response similar to that identified within hours¹⁹ of Hunga
 69 Tonga. This eruption thus represents an opportunity to quantify the wave response to a point-
 70 source disruption at a scale and comprehensiveness unique in the observational record.

71 Eruption and Immediate Wave Response

72 Figures 1 and 2 show the propagation of Lamb and gravity waves triggered by the initial
 73 eruption on the 15th of January, Figure 1 as height-integrated data from the Geostationary

74 Operational Environmental Satellite (GOES) and MeteoSat platforms and Figure 2 as height-
75 resolved measurements from multiple instrument types in addition to GOES.

76 The eruption became visible just after 04:00 UTC as a plume which reached a width of
77 200km and height of >30km within 30 minutes⁸. 20-30 minutes after the plume began rising,
78 a shockwave became visible in ten-minute-resolution near-infrared geostationary imagery.
79 Back-projection from surface pressure data shows that the trigger source occurred at 04:28±2
80 UTC, with the leading wavefront propagating away at a near-surface phase speed of 318.2±6
81 ms⁻¹ (Figure 2, Extended Data Figure 1c,d, Supplementary Figure 1). Based on the high phase
82 speed, large amplitude and non-dispersive nature of the signal we identify this as a Lamb
83 wave, i.e. a mixed packet of waves with non-dispersive wavelengths and periods travelling at
84 the same speed. This speed is consistent with the Lamb wave produced by Krakatoa,
85 estimated²⁰ to have propagated at 318.8±3 ms⁻¹.

86 The Hunga Tonga Lamb wave propagated around the globe, passing through the antipodal
87 point in Algeria 18.1 hours (±7.5 minutes) after the eruption (Figure 1). By this time, the
88 wavefront had deformed due to atmospheric and surface processes, and passed through the
89 antipode as four distinct wavefronts. Over following days, it was tracked propagating at least
90 three times²¹ around the Earth. We also see a faint signal in GOES data consistent with the
91 wave being partially reflected from the Andes on its first transit (Figure 1), and evidence of
92 the wave being slowed over South America (Supplementary Figure 2).

93 Using radiance data from the Advanced Infrared Sounder (AIRS), Cross-track Infrared
94 Sounder (CrIS) and Infrared Atmospheric Sounding Interferometer (IASI) polar-orbiting
95 thermal infrared (IR) sounders (specifically, 4.3µm data sensitive to altitudes ~39 km±5 km
96 and 15 µm data sensitive to the both ~25±5km and ~42±5km altitude levels separately,
97 Figure 2), we see the Lamb wave as a high-amplitude monochromatic pulse with a phase
98 speed of between 308±5 and 319±4 ms⁻¹ depending on location. We also observe it as a pulse
99 just above the noise floor of Cloud Imaging and Particle Size (CIPS) Rayleigh albedo data 12
100 300km away from and 10.75 hours after the eruption (~55±5km altitude, phase speed 316-
101 319 ms⁻¹, Extended Data Figure 4a), and as phase fronts in hydroxyl airglow over Hawai'i,
102 4960 km away from and 4.3 hours after (~87±4km altitude, phase speed 318 ms⁻¹).

103 The observed Lamb wave phase fronts are uniform in height and phase speed to within the
104 error range of each instrument from the surface to at least the upper mesosphere/lower
105 thermosphere. The energy density of a Lamb wave is theoretically expected²² to decay
106 exponentially with height, and the observed phase speed is consistent with a vertical mean of
107 sound speed weighted according to this energy distribution (see Methods). We observe a
108 slightly different speed for propagation in different directions across the Earth (e.g. at
109 Broome, Australia, we measure 319 ms⁻¹ for the westward-travelling wave and 316 ms⁻¹ for
110 the eastward, Extended Data Figure 1e), and the asymmetric perturbations we observe are
111 consistent in sign with such a shift due to background winds.

112 Following the Lamb wave, we observe a series of slower waves with continually varying
113 speeds and horizontal wavelengths (λ_h) that we identify as a dispersive packet of fast internal
114 gravity waves (Figure 2). These have phase speeds of 240-270 ms⁻¹, varying with local λ_h .
115 The leading phase front has the largest amplitude and longest λ_h , with a brightness
116 temperature (BT) amplitude of 0.74 K and λ_h of 380 km here falling to 0.15 K and 100 km
117 across the packet width. This packet is observed to extend ~2000 km and eight phase cycles

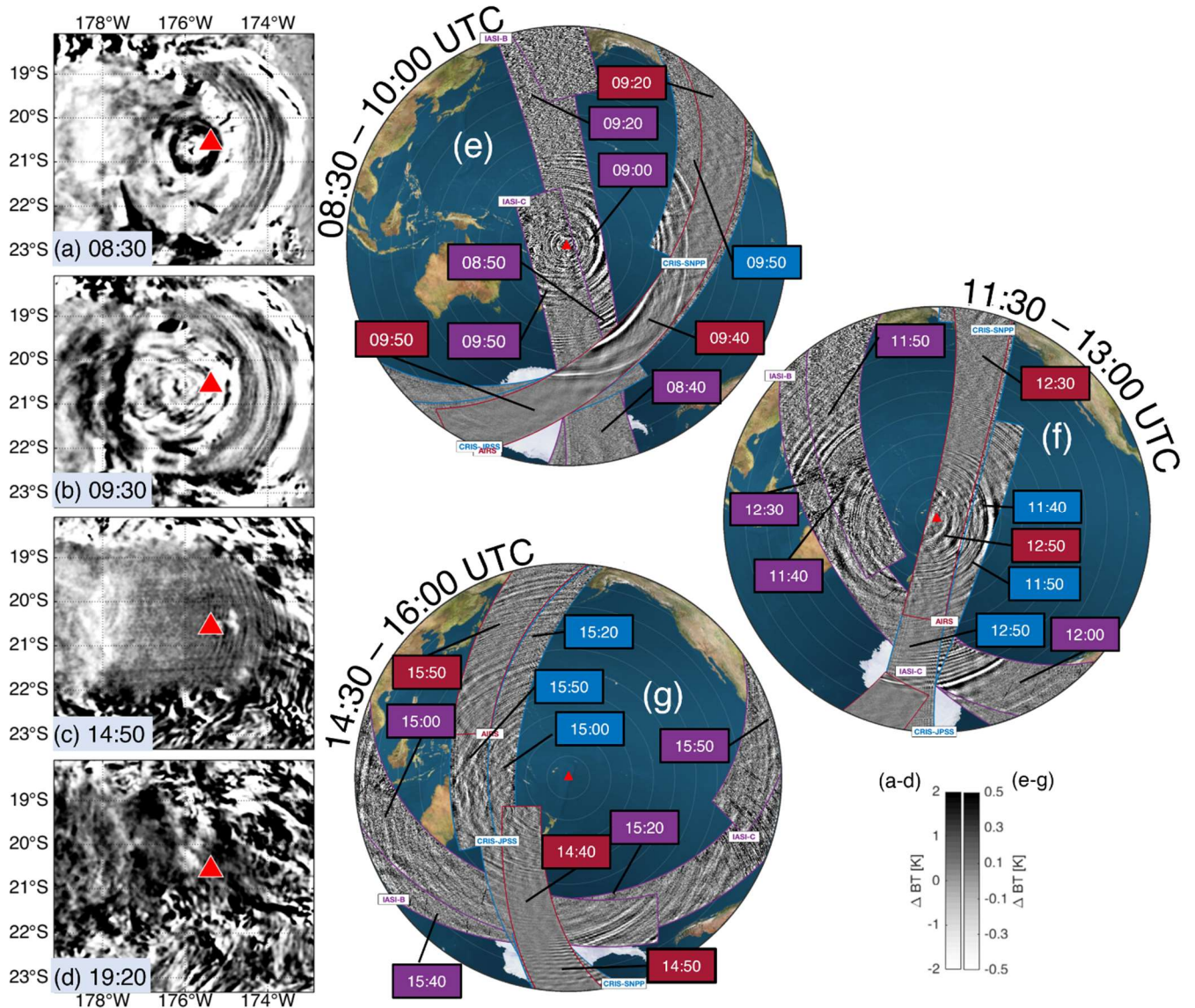


Figure 3: Post-eruption wave activity: (a-d) in and around the volcanic plume as observed by GOES and (e-g) over the entire Pacific basin as observed by AIRS, CrIS and IASI. For (e-g.) coloured labels indicate individual satellite overpass times for context, with AIRS labelled in red, CrIS in blue and IASI in purple. Note that the colour scales in panels (a) and (b) saturate significantly, and values extend to $\pm 8K$.

118 across the South Pacific ~ 7 hours after generation (Extended Data Figure 5). We observe the
 119 packet over multiple orbits of AIRS, CrIS, and IASI across the globe, in CIPS over
 120 Antarctica, and in airglow (~ 85 km altitude, depth ~ 8 km) above Hawai'i. Vertical wavelength
 121 (λ_z) is poorly defined but very deep: no phase difference is seen between AIRS observations
 122 at 25 and 42 km altitude, and calculations based on observed speed and λ_h imply $\lambda_z \gg 110$
 123 km, i.e. greater than the depth of the homosphere. These phase speeds are consistent with
 124 vertically-propagating gravity waves travelling at speeds close to, but very slightly less than,
 125 the theoretical maximum speeds achievable prior to total internal reflection (See Methods and
 126 Extended Data Figure 6) and with the same temporal origin and source as the Lamb wave.

127 This leading gravity wave packet passes through the antipode at times between $\sim 00:30$ and
 128 $02:30$ UTC, i.e. 20-22 hours after the eruption (Extended Data Figures 7a-c), with the broad

129 time window determined by separation of different λ_h components with time. Gravity waves
130 remaining coherent and expanding over the whole globe from a single source of any kind are
131 unprecedented in the observational record⁶. On their return journey from the antipode, the
132 waves become difficult to distinguish in our intermittent low-Earth orbit satellite snapshots
133 from those produced both later by Hunga Tonga and by other sources, and consequently we
134 cannot track them to their extinction.

135 The gap between the initial Lamb wave and subsequent gravity wave grows with time. This is
136 consistent with a theoretically-predicted forbidden phase speed range between external Lamb
137 wave and internal gravity wave limits imposed by total internal reflection (Extended Data
138 Figure 3). Two low-amplitude wavefronts are present in the gap; these propagate with the
139 same speed as the leading Lamb wavefront, but trace back to different origin times (Figure 2
140 and Extended Data Figure 5b). We therefore identify these as Lamb waves triggered by
141 subsequent smaller explosions which were also observed in local surface pressure (Extended
142 Data Figure 8).

143 Ionospheric data (Figure 2 and Extended Data Figure 3) show key differences from the lower
144 atmosphere. Over New Zealand, we see three large travelling ionospheric disturbances
145 (TIDs), with phase speeds, λ_h and amplitudes of (1) 667 ms⁻¹, 1000 km, 0.2 TEC Units
146 (TECu); (2) 414 ms⁻¹, 700 km, 0.4 TECu and (3) 343 ms⁻¹, 400 km and >1 TECu
147 respectively. They are consistent in speed and direction with a Hunga Tongan source
148 between 04:15 and 05:00, but do not share the arrival time, phase speed or λ_h of the Lamb
149 wave in other atmospheric layers. Therefore, we do not identify these TIDs as the Lamb
150 wave. However, a strong and brief TEC modulation, spiking at an amplitude of >0.6 TECu, is
151 seen at 6.15am consistent with the expected arrival time and brief period of the Lamb wave.

152 We do not see TID 1 over North America, but do see a signal consistent with TID 2 and
153 another TID (4) with phase speed ~311 m/s which is also consistent with TIDs measured over
154 New Zealand. We again see a strong TEC modulation at the expected Lamb wave arrival
155 time.

156 The properties of TIDs 1 and 2 are inconsistent with slant path gravity waves propagating
157 from Hunga Tonga, but could have reached the observed sites by indirect paths, e.g. by
158 vertically propagating as acoustic or gravity waves above the volcano then travelling at high
159 horizontal speeds through the ionosphere. The properties of TIDs 3 and 4 are consistent with
160 the wave activity generated over Hunga Tonga in the hours after the primary eruption.

161 **Sustained Post-Eruption Wave Generation**

162 After the initial trigger, sustained gravity wave generation is seen in the clouds above Hunga
163 Tonga and radiating outwards across the Pacific basin. While smaller in amplitude and slower
164 in phase speed than those from the initial eruption, these waves are also highly anomalous
165 relative to past gravity wave observations.

166 Figure 3 shows BT measurements from (a-d) the GOES 10.3 μ m channel over the Hunga
167 Tonga area and (e-g) the AIRS, CrIS and IASI 4.3 μ m stratospheric channels over the Pacific
168 basin for selected times.

169 In GOES observations of the eruption cloud top (Figure 3a-c, Supplementary Figure 3), arced
170 features consistent in morphology and temporal progression with propagating concentric
171 gravity wave phase fronts are visible. λ_h ranges from the 8km resolution limit of the data to
172 65km, and BT amplitude from 0.5-8K. These measured properties are very similar to those of
173 gravity waves generated near the convective centres of hurricanes.

174 The apparent centre of these waves is slightly west of Hunga Tonga. This is consistent with
175 refraction of the wave field by the prevailing easterly winds. The waves are remarkably
176 consistent in concentric shape over several hours, suggesting a powerful and relatively
177 persistent pulsing source for wave generation. The source may be pulses of convection
178 within the plume above the volcano. The waves weaken in amplitude over time, particularly
179 after 15:00UTC, but are visible until at least 19:20 UTC (Figure 3d). They are not found on
180 subsequent days. These results suggest that the volcano may have created a sustained source
181 of convectively-generated waves for nearly fifteen hours after the initial eruption

182 Stratospheric AIRs, CrIS and IASI observations (Figure 3e-g, Extended Data Figure 7d-o)
183 show wave activity across a range of spatial, frequency and amplitude scales throughout the
184 Pacific basin, all centred on Hunga Tonga. Tracking individual phase fronts is challenging as
185 these data are near-instantaneous at any given location, but conservatively the distribution
186 must include a large fraction of waves with phase speeds $>100 \text{ ms}^{-1}$. For example, small-scale
187 continuous wavefronts centred on Hunga Tonga are clearly visible near Japan before 16:00 in
188 Figure 3g and, even if emitted at the earliest possible time of 04.28 UTC, must have phase
189 speeds $\sim 200 \text{ ms}^{-1}$ to have travelled this far. Unlike more typical observed waves, these waves
190 can therefore propagate with little apparent influence from global wind patterns due to their
191 unusually large phase speeds. Such fast speeds reduce normal dissipation effects, allowing
192 the waves to propagate vast distances and affect much higher altitudes than typical gravity
193 waves.

194 These waves dominate the stratospheric gravity wave spectrum over a radius $>9000\text{km}$ for
195 >12 hours (Extended Data Figure 7d-o). This is exceptional for a single source, and unique in
196 our observational record^{6,7}. Orographic wave sources often persist for longer, but are spatially
197 localised; while some waves in the southern polar jet may have propagated downstream^{23,24}
198 or laterally^{6,25} from orographic sources, the area they affect is an order of magnitude smaller
199 than here and the waves themselves highly intermittent. Waves from non-orographic sources
200 such as tropical convection and extreme events such as hurricanes, meanwhile, typically
201 become indistinguishable from background within 2000-3500 km²⁶⁻²⁷.

202 **How were the waves generated?**

203 Although we cannot directly observe the generation of the waves due to insufficient temporal
204 resolution (for the initial explosion) and ash plume blocking effects (for both the initial
205 explosion and subsequent wave generation), the observed wave properties and context allow
206 us to infer likely mechanisms by which they were generated.

207 The strong initial response is likely due to the eruption's shallow submarine context and large
208 explosive power. As the volcanic vent was only tens to hundreds of metres below water²⁸ the
209 seawater did not suppress the blast but was instead flash-boiled²⁹ and propelled into the
210 stratosphere. Here it condensed, releasing latent heat near-instantaneously across a depth of
211 tens of kilometres. This strong and short-lived forcing would produce vertically-deep waves
212 across a broad spectrum, consistent with observations. This mechanism is also consistent with
213 significant and large IASI-observed increases in stratospheric water vapour (Extended Data
214 Figure 9), and H_2SO_4 in the plume relative to what would be expected for an eruption of this
215 size, which is in turn consistent with sulfuric acid forming in situ due to insufficient
216 volcanogenic SO_2 release and the time available to produce H_2SO_4 .

217 Subsequent wave generation is likely due to similar processes as standard convective waves,
218 such as mechanical oscillator effects³⁰ associated with vertical air motion within the plume or
219 pulsing from the volcanic heat source below. Such forces would produce sufficiently strong
220 perturbations to generate gravity waves visible both in the plume and propagating freely

221 away. Such a mechanism is again consistent with our observations, particularly the similarity
222 in morphology and amplitude of the observed waves to those generated by hurricanes and
223 convective weather systems.

224 **Weather and Climate Forecasting Implications**

225 While in recent years we have been able to routinely characterise gravity waves in
226 observational data, understanding how the observed spectrum at a location arises has been
227 complicated by fundamental problems in distinguishing the source of a wave from the
228 pathway it has taken to the observation²⁴. Being able to separate these problems would lead to
229 major advances in simulating and parameterising gravity waves in next-generation weather
230 and climate models.

231 The Hunga Tonga eruption represents an important natural experiment in this area. The
232 volcano was a clearly-identifiable near-point source, produced gravity waves across a broad
233 range of spatiotemporal and frequency scales, and these waves were observed by a diverse
234 constellation of instruments worldwide. As such, simulating this eruption in atmospheric
235 models, whether as a point convective source or in a dedicated volcanic simulation, could
236 provide major insight into the strengths and deficiencies of models. In addition, comparison
237 of modelled and observed propagation delays for both the Lamb and gravity waves will
238 provide important information quantifying how well current and future models represent
239 atmospheric winds, temperatures and density structures.

240

241 **Main References**

- 242 1. Poli, P. & Shapiro, N. M. Rapid characterization of large volcanic eruptions: measuring
243 the impulse of the Hunga Tonga explosion from teleseismic waves.
244 <http://www.essoar.org/doi/10.1002/essoar.10510358.1> (2022)
245 doi:10.1002/essoar.10510358.1.
- 246 2. Pyle, D. M. Sizes of Volcanic Eruptions. in *The Encyclopedia of Volcanoes* 263–269
247 (Elsevier, 2000).
- 248 3. Garrett, C. J. R. Atmospheric edge waves. *Q.J Royal Met. Soc.* **95**, 731–753 (1969).
- 249 4. The Eruption of Krakatoa and Subsequent Phenomena. *Q.J.R. Meteorol. Soc.* **14**, 301–307
250 (1888).
- 251 5. Fritts, D. C. & Alexander, M. J. Gravity wave dynamics and effects in the middle
252 atmosphere. *Rev. Geophys.* **41**, 1003 (2003).
- 253 6. Hindley, N. P., Wright, C. J., Hoffmann, L., Moffat-Griffin, T. & Mitchell, N. J. An 18-
254 Year Climatology of Directional Stratospheric Gravity Wave Momentum Flux From 3-D
255 Satellite Observations. *Geophys. Res. Lett.* **47**, (2020).
- 256 7. Ern, M. et al. GRACILE: a comprehensive climatology of atmospheric gravity wave
257 parameters based on satellite limb soundings. *Earth Syst. Sci. Data* **10**, 857–892 (2018).
- 258 8. Carr, J. L., Horvath, A., Wu, D. L. & Friberg, M. D. Stereo Plume Height and Motion
259 Retrievals for the Record-Setting Hunga Tonga-Hunga Ha’apai Eruption of 15 January
260 2022. <http://www.essoar.org/doi/10.1002/essoar.10510365.1> (2022)
261 doi:10.1002/essoar.10510365.1.
- 262 9. Press, F. & Harkrider, D. Air-Sea Waves from the Explosion of Krakatoa. *Science* **154**,
263 1325–1327 (1966).
- 264 10. Pfeffer, R. L. & Zarichny, J. Acoustic-Gravity Wave Propagation from Nuclear
265 Explosions in the Earth’s Atmosphere. *J. Atmos. Sci.* **19**, 256–263 (1962).
- 266 11. Kanamori, H. & Given, J. W. Lamb pulse observed in nature. *Geophys. Res. Lett.* **10**,
267 373–376 (1983).

- 268 12. Miller, S. D. et al. Upper atmospheric gravity wave details revealed in nightglow satellite
269 imagery. *Proc Natl Acad Sci USA* **112**, E6728–E6735 (2015).
- 270 13. Widmer, R. & Zürn, W. Bichromatic excitation of long-period Rayleigh and air waves by
271 the Mount Pinatubo and El Chichon volcanic eruptions. *Geophys. Res. Lett.* **19**, 765–768
272 (1992).
- 273 14. De Angelis, S., McNutt, S. R. & Webley, P. W. Evidence of atmospheric gravity waves
274 during the 2008 eruption of Okmok volcano from seismic and remote sensing
275 observations: Gravity Waves at Okmok Volcano. *Geophys. Res. Lett.* **38** (2011).
- 276 15. Watada, S. & Kanamori, H. Acoustic resonant oscillations between the atmosphere and
277 the solid earth during the 1991 Mt. Pinatubo eruption. *J. Geophys. Res.* **115**, B12319
278 (2010).
- 279 16. Astafyeva, E. Ionospheric Detection of Natural Hazards. *Rev. Geophys.* 2019RG000668
280 (2019) doi:10/gghhwc.
- 281 17. Themens, D. R. et al. Global propagation of ionospheric disturbances associated with the
282 2022 Tonga Volcanic Eruption. <http://www.essoar.org/doi/10.1002/essoar.10510350.1>
283 (2022) doi:10.1002/essoar.10510350.1.
- 284 18. Manta, F. et al. Correlation Between GNSS-TEC and Eruption Magnitude Supports the
285 Use of Ionospheric Sensing to Complement Volcanic Hazard Assessment. *J Geophys Res*
286 *Solid Earth* **126**, (2021).
- 287 19. Adam, D. Tonga volcano eruption created puzzling ripples in Earth’s atmosphere. *Nature*
288 d41586-022-00127–1 (2022) doi:10/gn8ktd.
- 289 20. Taylor, G. I. Waves and tides in the atmosphere. *Proc. R. Soc. Lond. A* **126**, 169–183
290 (1929).
- 291 21. Lin, J.-T. et al. Rapid Conjugate Appearance of the Giant Ionospheric Lamb Wave in the
292 Northern Hemisphere After Hunga-Tonga Volcano Eruptions.
293 <http://www.essoar.org/doi/10.1002/essoar.10510440.1> (2022)
294 doi:10.1002/essoar.10510440.1.
- 295 22. Bretherton, F. P. Lamb waves in a nearly isothermal atmosphere. *Q.J Royal Met. Soc.* **95**,
296 754–757 (1969).
- 297 23. Hindley, N. P., Wright, C. J., Smith, N. D. & Mitchell, N. J. The southern stratospheric
298 gravity wave hot spot: individual waves and their momentum fluxes measured by
299 COSMIC GPS-RO. *Atmos. Chem. Phys.* **15**, 7797–7818 (2015).
- 300 24. Wright, C. J., Hindley, N. P., Hoffmann, L., Alexander, M. J. & Mitchell, N. J. Exploring
301 gravity wave characteristics in 3-D using a novel S-transform technique: AIRS/Aqua
302 measurements over the Southern Andes and Drake Passage. *Atmos. Chem. Phys.* **17**,
303 8553–8575 (2017).
- 304 25. Plougonven, R., la Cámara, A., Hertzog, A. & Lott, F. How does knowledge of
305 atmospheric gravity waves guide their parameterizations? *Q.J.R. Meteorol. Soc* **146**,
306 1529–1543 (2020).
- 307 26. Wright, C. J. Quantifying the global impact of tropical cyclone-associated gravity waves
308 using HIRDLS, MLS, SABER and IBTrACS data. *Q.J.R. Meteorol. Soc.* **145**, 3023–3039
309 (2019).
- 310 27. Stephan, C. & Alexander, M. J. Realistic simulations of atmospheric gravity waves over
311 the continental U.S. using precipitation radar data. *J. Adv. Model. Earth Syst.* **7**, 823–835
312 (2015).
- 313 28. Colombier, M. et al. Vesiculation and Quenching During Surtseyan Eruptions at Hunga
314 Tonga-Hunga Ha’apai Volcano, Tonga. *J. Geophys. Res. Solid Earth* **123**, 3762–3779
315 (2018).

- 316 29. Witze, A. Why the Tongan eruption will go down in the history of volcanology. Nature
317 d41586-022-00394-y (2022) doi:10/gpfhem.
318 30. Fovell, R., Durran, D. & Holton, J. R. Numerical Simulations of Convectively Generated
319 Stratospheric Gravity Waves. J. Atmos. Sci. **49**, 1427–1442 (1992).

320

321

322 **Tables**

323 [none]

324

325 **Methods**

326 **Explosive Energy Estimate from Surface Pressure Data**

327 We estimate the explosive energy associated with the eruption using three separate
328 approaches. All three give a value in the range 10-28 EJ.

329 1. Waveform based on a nuclear explosion: Posey and Pierce (1971)³³ suggested that the
330 energy yield of an explosion in the atmosphere can be calculated as $E = 13p\sqrt{[r_e \sin(r/$
331 $r_e)]H_s(CT)^{3/2}$, where p is the measured pressure anomaly, r the distance from the explosion,
332 r_e the Earth's radius, H_s the atmospheric scale height, c the speed of the wave, and T the time
333 separation between the first and second peaks of the pressure disturbance. From available
334 pressure-station data at distances ranging from 2500-17500 km from Hunga Tonga (Extended
335 Data Figure 1b), this provides an estimate $\sim 20 \pm 8$ EJ.

336 2. Waveform based on previous volcanic eruptions: Gorshkov (1960)³⁴ estimated the
337 explosive energy of a volcanic eruption as $E = \frac{2\pi H_s \sin(\theta)}{\rho c} \int p^2 dt$, where θ is the distance
338 from the eruption in degrees and ρ the Earth's surface air density, and t is time. This gives an
339 estimate of ~ 10 EJ.

340 3. Estimated pressure force: assuming the pressure anomaly spreads under an even cloud of
341 area A , then the work done by the pressure impulse over a column of height h_c is $W = pAh_c$.
342 For an area of radius 200 km and pressure change of 5 hPa, this gives a work estimate ~ 18
343 EJ.

344

345 **Estimate of Lamb Wave Phase Speed**

346 We use the approach of Bretherton (1969)²² and initial-release data from the European Centre
347 for Medium-Range Weather Forecasts' Fifth-Generation Reanalysis (ERA5T) to calculate the
348 expected speed of the Lamb wave. We first compute the local speed of sound as $c_s(z) =$
349 $20.05\sqrt{T}$, where z is the altitude and T the local temperature. For a Lamb wave, where energy
350 density decays exponentially with height, energy density is $E(z) = C \exp(-z/H)$, where C
351 is a constant term which subsequently cancels in our calculation, and H is

$$352 \quad H = \frac{c_s^2}{(2-\gamma)} g,$$

353 for a ratio of specific heats γ which we set to 1.4, and acceleration due to gravity g which we
354 set to 9.80665ms^{-1} . We then calculate the phase speed of the Lamb wave as a vertical mean of
355 the speed of sound weighted by energy density, i.e.

$$356 \quad c_m^2 = \frac{\int [c_s(z)+u(z)]^2 E(z) dz}{\int E(z) dz},$$

357 where u is the local wind speed.

358 For ERA5T meteorological output for the 15th of January 2022 at the 04:00 UTC timestep,
359 this gives a phase speed of $313\text{-}318 \text{ms}^{-1}$. Similar results are obtained using the 05:00 UTC
360 timestep. Our calculation omits the contribution of altitudes above 80 km to the energy
361 density calculation as ERA5 data do not extend above this level, but as energy density
362 decreases exponentially with height this contribution should be small.

363

364 Gravity Wave Speed Limit Calculation

365 Linear wave solutions to the Navier-Stokes equations of the form $A \exp[(i(kx + mz + \hat{\omega}t))]$
366 satisfy the dispersion relation [22] of Fritts and Alexander (2003)⁵, which is fourth-order in
367 intrinsic frequency $\hat{\omega}$. For higher-frequency waves where $f^2 \ll \hat{\omega}^2$ and simplifying to planar
368 2D propagation, i.e. $l = 0$, we can rewrite this as a fourth-order equation in intrinsic phase
369 speed $\hat{c} = \hat{\omega}/k$, i.e.

$$370 \quad \frac{\hat{c}^4}{c_s^2} - \hat{c}^2 \left(1 + \frac{1}{4H^2 k^2} + \frac{m^2}{k^2} \right) + \frac{N^2}{k^2} = 0.$$

371 Letting $x = \hat{c}^2$ gives a quadratic form of the equation

$$372 \quad ax^2 + bx + c = 0$$

373 where $a = 1/c_s^2$, $b = -(1 + 1/(4H^2 k^2) + m^2/k^2)$ and $c = N^2/k^2$, with solution

$$374 \quad \hat{c}^2 = \frac{-b \pm \sqrt{b^2 - 4a}}{2a}.$$

375 Allowing vertical wavenumber $m \rightarrow 0$ gives the curve $\hat{c}_{max}(k)$, the maximum phase speed
376 for gravity waves before total internal reflection would prevent their vertical propagation.
377 This limit is

$$378 \quad \hat{c}_{max}^2 = \frac{c_s^2}{2} \left[1 + (4H^2 k^2)^{-1} - \sqrt{[1 + 1/(4H^2 k^2)]^2 - 4N^2/(c_s^2 k^2)} \right]$$

379 and is shown as a function of horizontal wavelength k^{-1} in Extended Data Figure 6. Our
380 results for the wave properties produced by Hunga Tonga are consistent with previous
381 theoretical work considering normalised full spectra of acoustic and gravity waves³⁵.

382 Airglow Imagery Processing

383 Airglow data have been obtained from the all-night cloud cameras at the Gemini Observatory
384 on Mauna Kea, Hawaii. Images have been converted from original northward and upward
385 viewing camera angles to an overhead latitude-longitude grid by visual identification of
386 multiple bright stars in the image fields-of-view, then a geometric conversion to give the
387 position of each pixel on the sky at the 87km airglow layer we assume to contain the waves.
388 This assumed height layer is based on the colour of the airglow and spectral range of the
389 cameras used at Gemini, which are both consistent with the hydroxyl (OH) airglow layer.

390 AIRS, CRIS and IASI

391 We use brightness temperature observations associated with radiances in the 4.3 μm and 15
392 μm carbon dioxide absorption bands of AIRS, CrIS, IASI-B and IASI-C³¹ on the 15th of
393 January. These instruments can directly resolve stratospheric waves with vertical
394 wavelengths $\gtrsim 15\text{km}$ and horizontal wavelengths $\gtrsim 30\text{km}$, and typically provide twice-daily
395 near-global coverage for each instrument in near-real time with an orbit approximately every
396 90 minutes. Perturbation fields suitable for spectrally and visually analysing wave signatures
397 are produced by subtracting a fourth-order polynomial in the across-track direction from the
398 data, consistent with previous work using these data^{6,32}.

399 CIPS

400 Imagery from the nadir-viewing CIPS instrument is analysed for the presence of deviations
401 from a smooth model background of Rayleigh scattered UV sunlight (265 nm). The model

402 removes the geometrical dependence of the observation and large-scale geophysical
403 variability of the observed albedo. The data are binned to a uniform 7.5x7.5 km grid,
404 allowing for observations down to 15 km horizontal wavelength. The altitude kernel limits
405 sensitivity to vertical wavelengths ≥ 10 km, with peak contribution at ~ 50 km altitude. The
406 satellite is in a sun synchronous polar orbit with an equator crossing currently near noon.

407 **GOES/MeteoSat**

408 We use data from band 13 of GOES-EAST and GOES-WEST, and band 5 of Meteosat-
409 SEVIRI. These instruments image the Earth's disc at a spatial resolution of 2 km and a
410 temporal resolution of 10 minutes (15 minutes for SEVIRI). Raw radiance data have been
411 converted to brightness temperatures based on the centre wavelength of the channels filters,
412 and then differenced between adjacent timesteps to highlight wave structure.

413 **TEC**

414 Total electron content observations were derived from dual-frequency GPS receivers in the
415 New Zealand GeoNet and the NOAA CORS Networks. Satellite to ground GPS signals were
416 processed following the method of Afraimovich et al (2000)³⁶, and the dTEC values are
417 projected onto an ionospheric shell altitude of 250 km. The dTEC are then analysed to
418 investigate the travelling ionospheric disturbance parameters.

419 **Data Availability**

420 Airglow data are available from from <https://www.gemini.edu/sciops/telescopes-and-sites/weather/mauna-kea/cloud-cam/allnightlong.html>. They were obtained under a Creative
421 Commons Attribution 4.0 International License issued by the NSF's NoirLab.
422

423 AIRS and CrIS data are available from the NASA Goddard Earth Sciences Data and
424 Information Services Center: <https://disc.gsfc.nasa.gov/>.

425 CIPS data are available from the Laboratory for Atmospheric and Space Physics at the
426 University of Colorado Boulder: <https://lasp.colorado.edu/aim/>.

427 ERA5 data are available from the Climate Data Store, <https://cds.climate.copernicus.eu>.

428 GOES data are available from the NOAA Geostationary Satellite Server,
429 <https://www.goes.noaa.gov/>.

430 IASI data are available from the IASI Portal, <https://iasi.aeris-data.fr/>.

431 Surface Pressure data are included as a Supplementary file to this manuscript.

432 TEC data are available from <https://www.geonet.org.nz/> and <https://geodesy.noaa.gov/CORS/>

433 **Methods References**

434 31. Hoffmann, L. et al. Intercomparison of stratospheric gravity wave observations with
435 AIRS and IASI. *Atmos. Meas. Tech.* **7**, 4517–4537 (2014).

436 32. Alexander, M. J. & Barnet, C. Using Satellite Observations to Constrain
437 Parameterizations of Gravity Wave Effects for Global Models. *Journal of the Atmospheric*
438 *Sciences* **64**, 1652–1665 (2007).

439 33. Posey, J. W. & Pierce, A. D. Estimation of Nuclear Explosion Energies from
440 Microbarograph Records. *Nature* **232**, 253–253 (1971).

441 34. Gorshkov, G. S. Determination of the explosion energy in some volcanoes according to
442 barograms. *Bull Volcanol* **23**, 141–144 (1960).

- 443 35. Yeh, K. C. & Liu, C. H. Acoustic-gravity waves in the upper atmosphere. *Rev. Geophys.*
444 **12**, 193 (1974).
445 36. Afraimovich, E.L. et al. Observation of large-scale traveling ionospheric disturbances of
446 auroral origin by global GPS networks/. *Earth, Planets and Space* **52** 669-674 (2000)
447 37. Hindley, N. P., Smith, N. D., Wright, C. J., Rees, D. A. S. & Mitchell, N. J. A two-
448 dimensional Stockwell transform for gravity wave analysis of AIRS measurements.
449 *Atmos. Meas. Tech.* **9**, 2545–2565 (2016).

450

451 **Code Availability**

452 All software used is either already publicly available, implements equations provided in the
453 Methods section directly, or only plots data.

454 **Acknowledgements**

455 CJ Wright is supported by a Royal Society University Research Fellowship, reference
456 UF160545. CJ Wright and NP Hindley are supported by NERC grant NE/S00985X/1.
457 MJ Alexander and CE Randall are supported by a NASA Heliophysics DRIVE Science
458 Center (grant no. 80NSSC20K0628). CN Mitchell was supported by NERC Fellowship
459 NE/P006450/1 for work underpinning this research. C Clerbaux and M Bouillon received
460 funding from the European Research Council (ERC) under the European Union’s Horizon
461 2020 and innovation programme (grant agreement No 742909, IASI-FT advanced ERC
462 grant). The Australian Institute of Marine Sciences, the Australian Bureau of Meteorology
463 and the Tongan Met Office are thanked for provision of surface station pressure data. The
464 authors would like to thank Isabell Krisch, Natalie Kaifler and Bernd Kaifler (all at the DLR,
465 Oberpfaffenhofen, Germany) for assistance with preliminary data analysis and Ed Gryspeerdt
466 (Imperial College, London, UK) for independent confirmation of the Lamb wave trigger
467 time.

468 **Author Contributions**

469 Conceptualisation: Wright, Hoffmann, Osprey
470 Data curation: Hoffmann, Bouillon, Carsten, Clerbaux, Mitchell, Randall
471 Formal analysis: Hindley, Alexander, Barlow, Mitchell, Prata, Hoffmann
472 Funding acquisition: Wright, Clerbaux
473 Investigation: All
474 Methodology: Wright, Hindley, Alexander, Barlow, Mitchell, Prata, Hoffmann
475 Software: Wright, Hindley, Alexander, Barlow, Mitchell, Prata, Hoffmann
476 Administration: Wright
477 Visualisation: Wright, Hindley, Alexander, Barlow, Prata
478 Writing – original draft: Wright
479 Writing: review/editing: Alexander, Hoffmann, Mitchell, Osprey

480

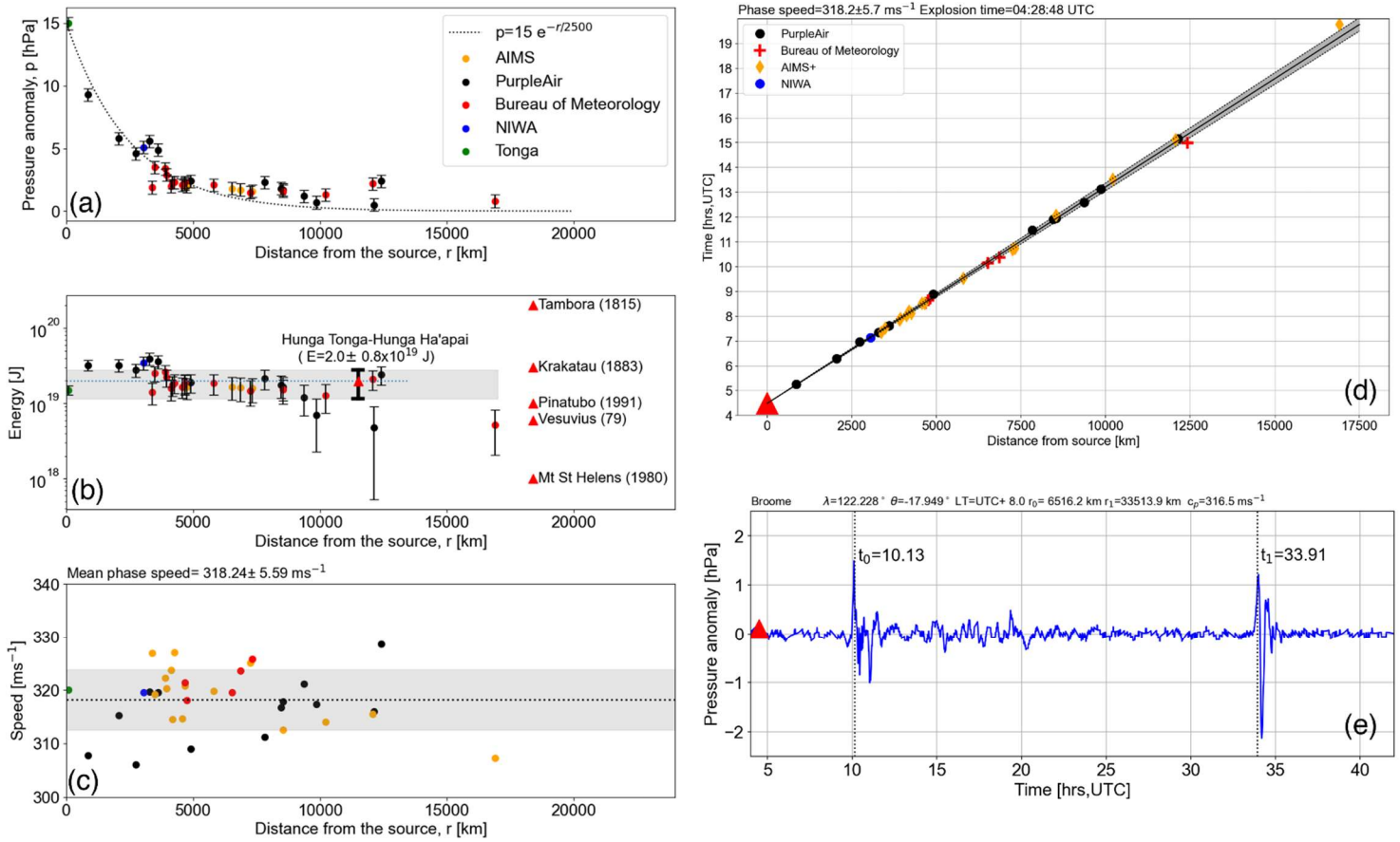
481 **Competing Interest Declaration**

482 The authors declare no competing interests.

483 **Additional Information**

484 Correspondence to Corwin Wright, c.wright@bath.ac.uk.

485 **Extended Data**

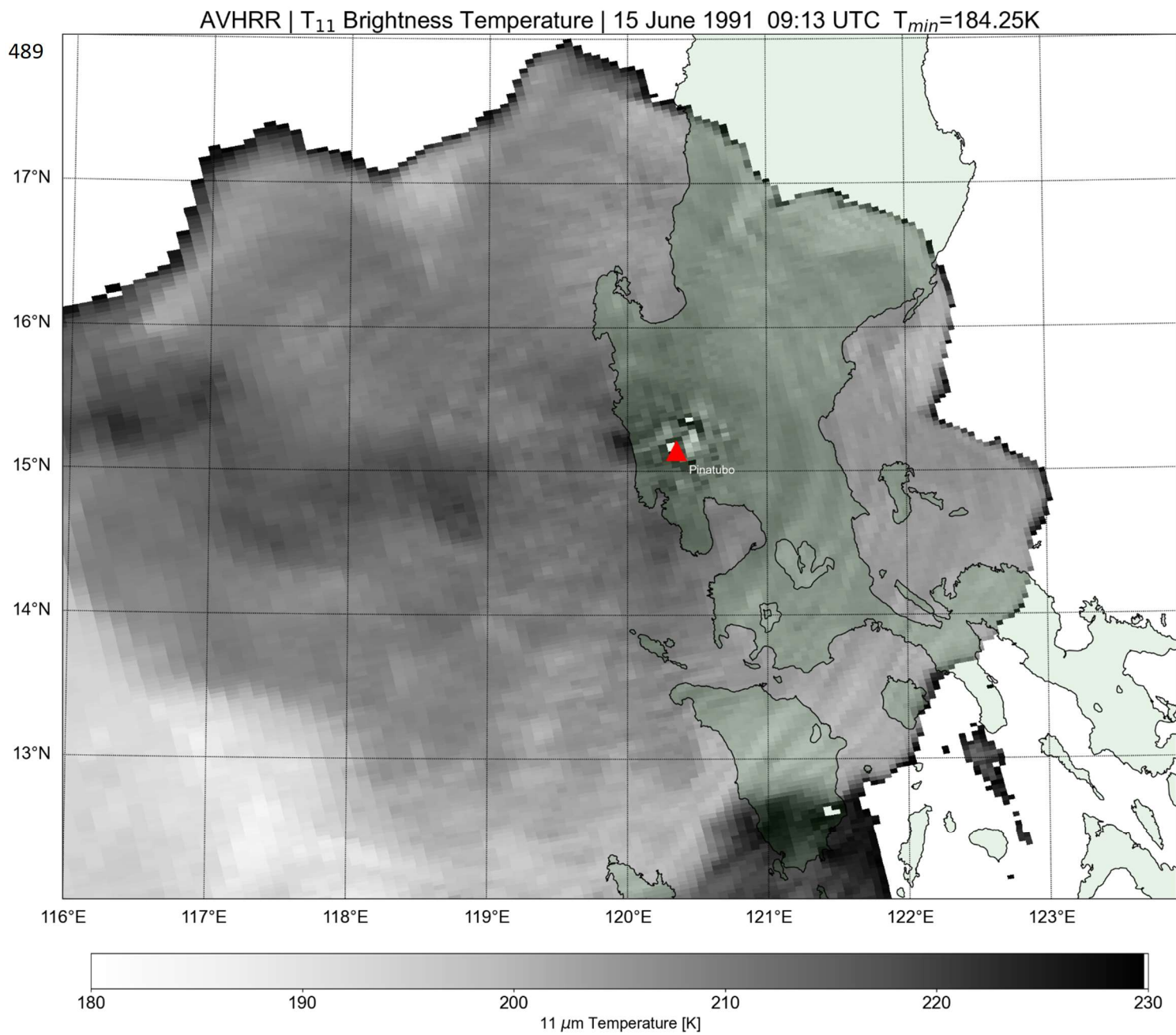


486

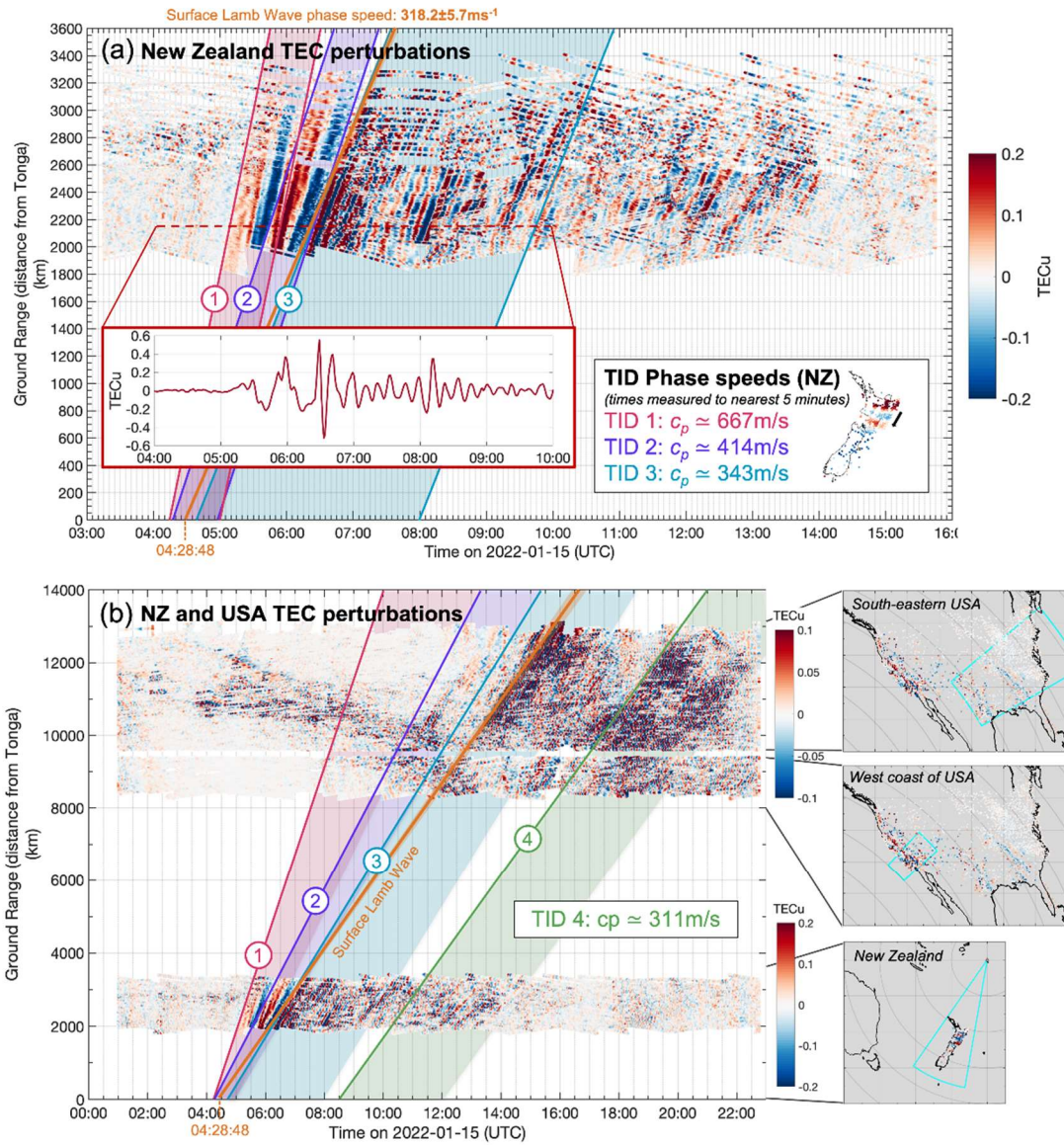
Extended Data Figure 1: (a-d) Estimates of (a) Lamb-wave-induced pressure anomaly, (b) eruption explosive energy, (c) Lamb wave phase speed and (d) time of primary explosion, as computed from surface pressure data. (e) Time series of measured pressure anomaly at Broome, Australia.

487

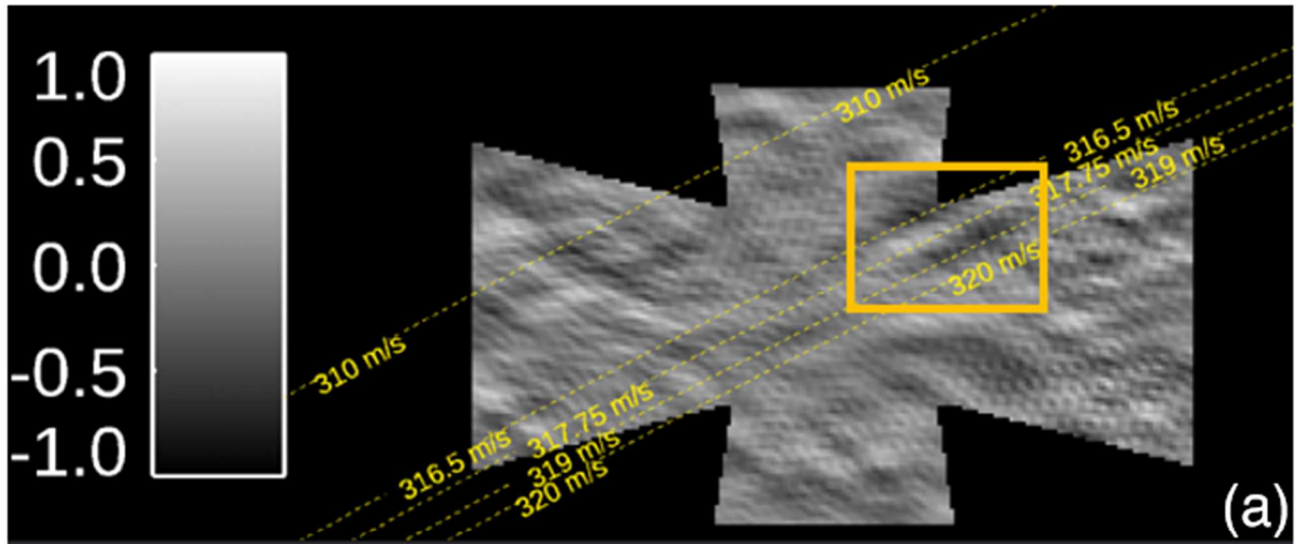
488



Extended Data Figure 2: Brightness temperature measures over the 1991 Pinatubo eruption plume, as observed by the Advanced Very High Resolution Radiometer.

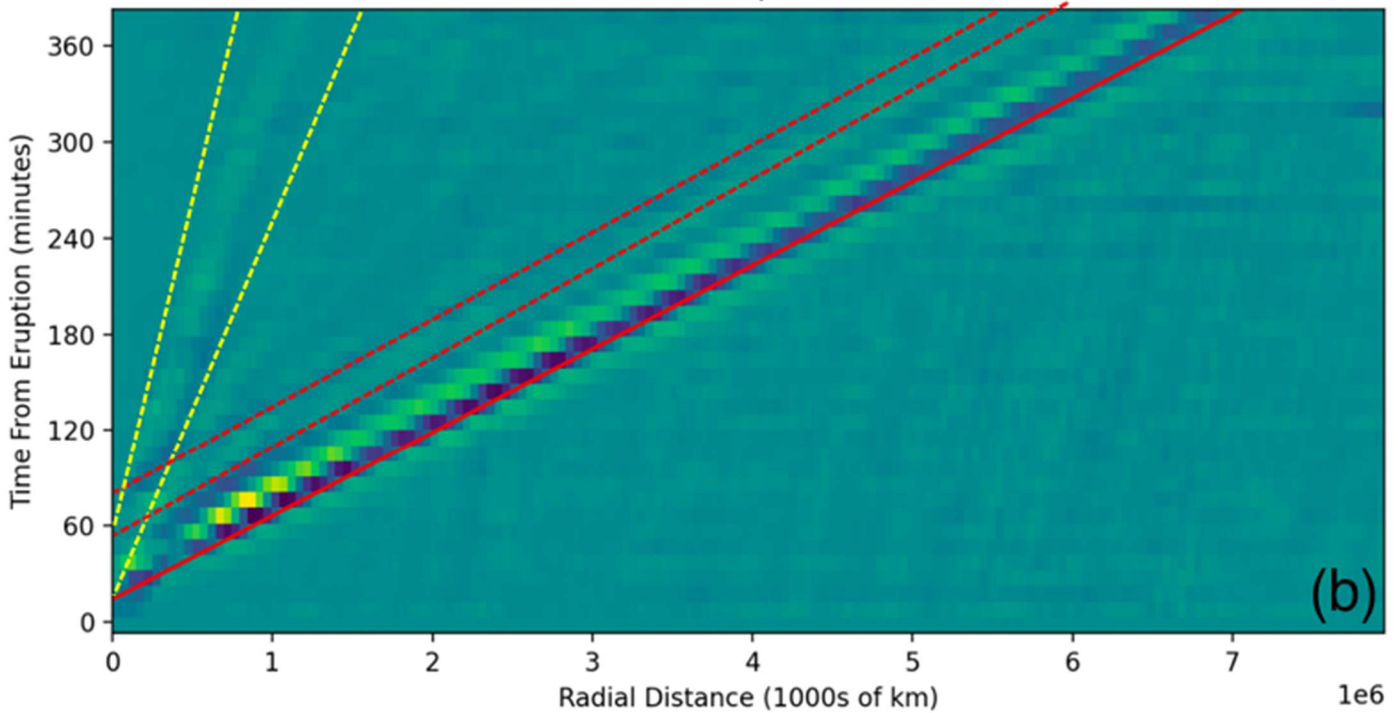


Extended Data Figure 3: Time-distance plots of ionospheric disturbances over New Zealand and the United States, computed from GNSS-TEC data.



(a)

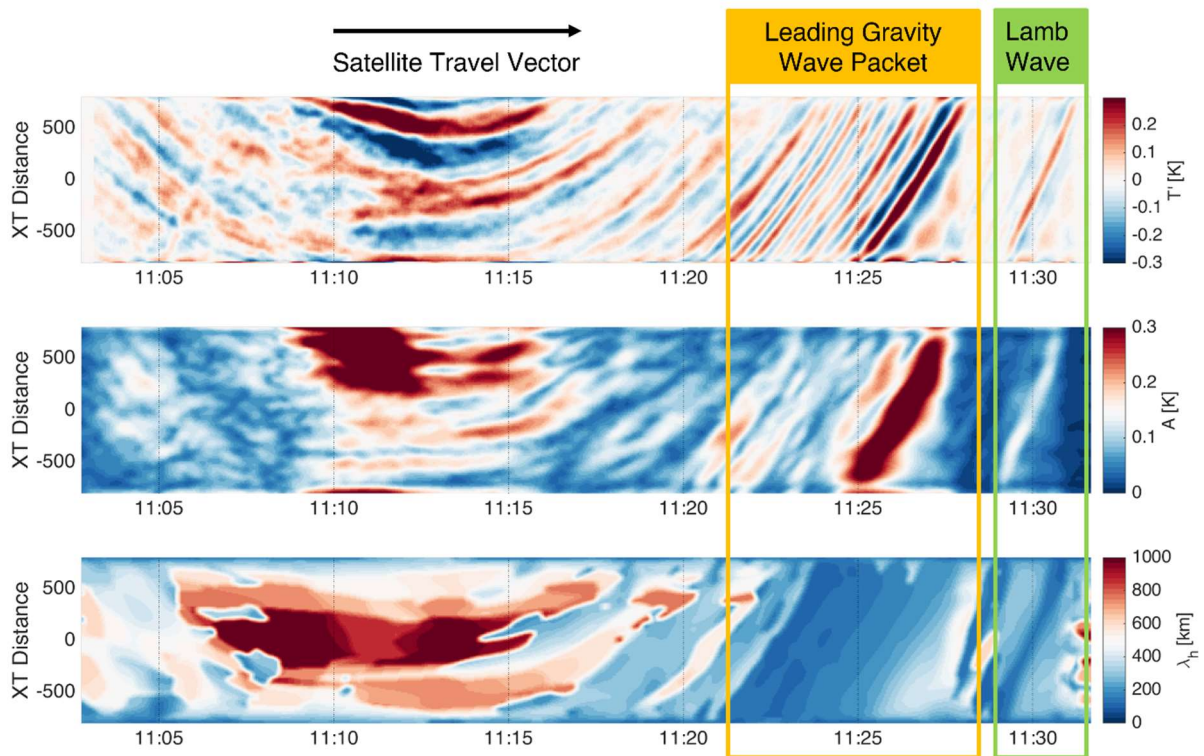
Time - Distance Plot of Eruption in GOES-W Band 13



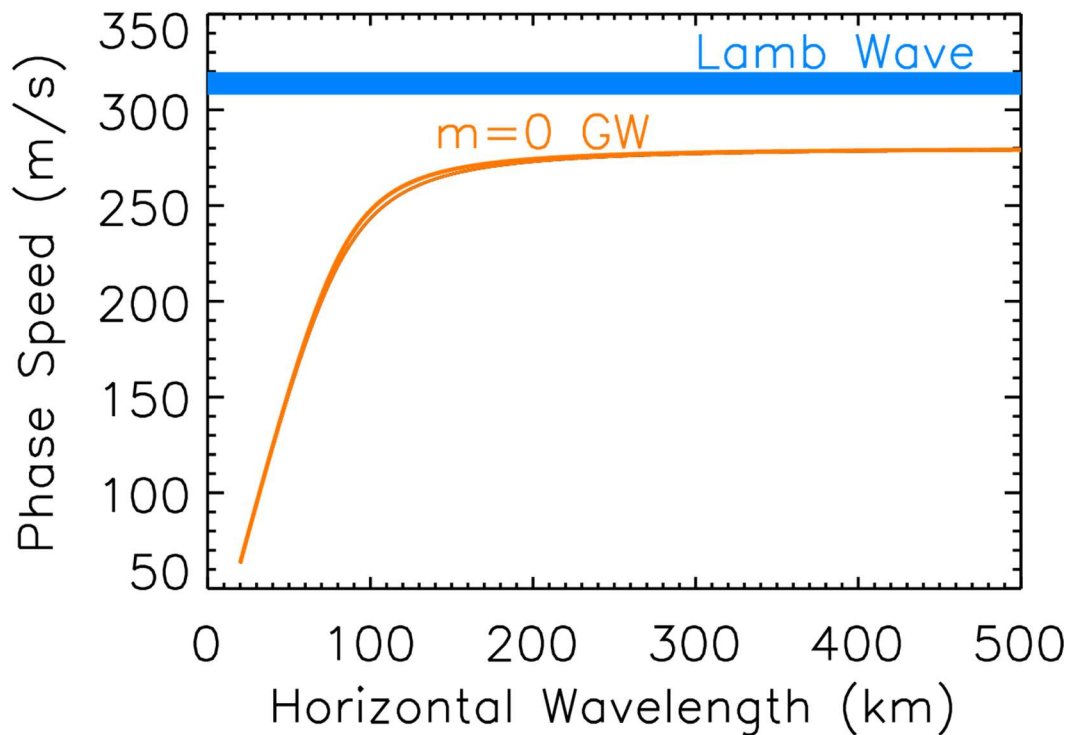
(b)

491

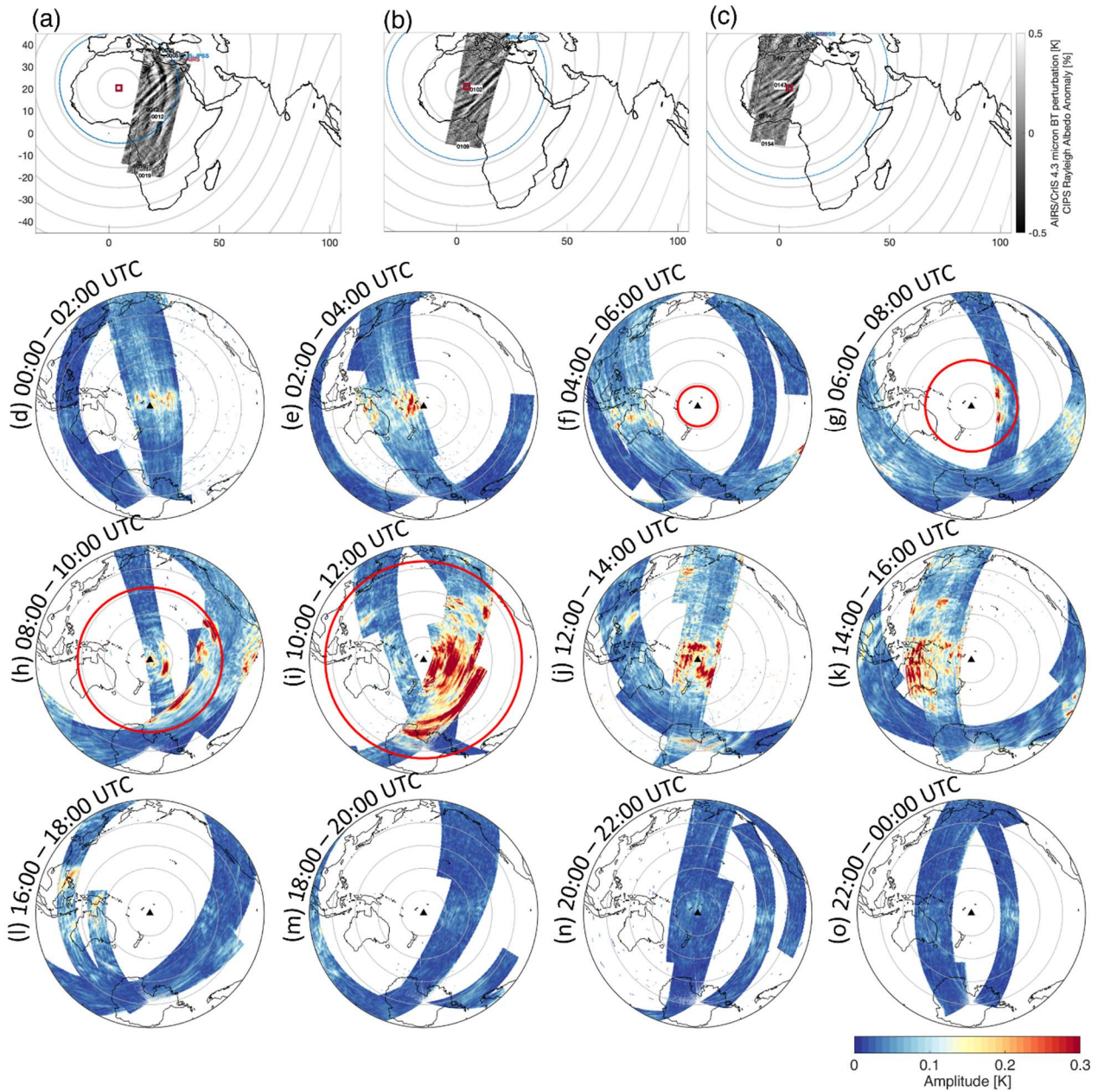
Extended Data Figure 4: (a) Lamb wave as observed by CIPS (centred at 24°S 309°E, 12300 from Hunga Tonga, and recorded 10.75 hours after the eruption). In these data, the Lamb wave is extremely close to the instrument noise floor and statistical tests were carried out to confirm that the small signal seen is consistent with the expected speed and wavelength of the Lamb wave. (b) Time-distance spectrum derived from GOES 10um channel, with Hunga Tonga located at the origin. Red solid line identifies the primary Lamb wave, red dashed lines weaker secondary Lamb waves, and yellow dashed lines outline the limits of the dispersive gravity waves in the initially-released packet.



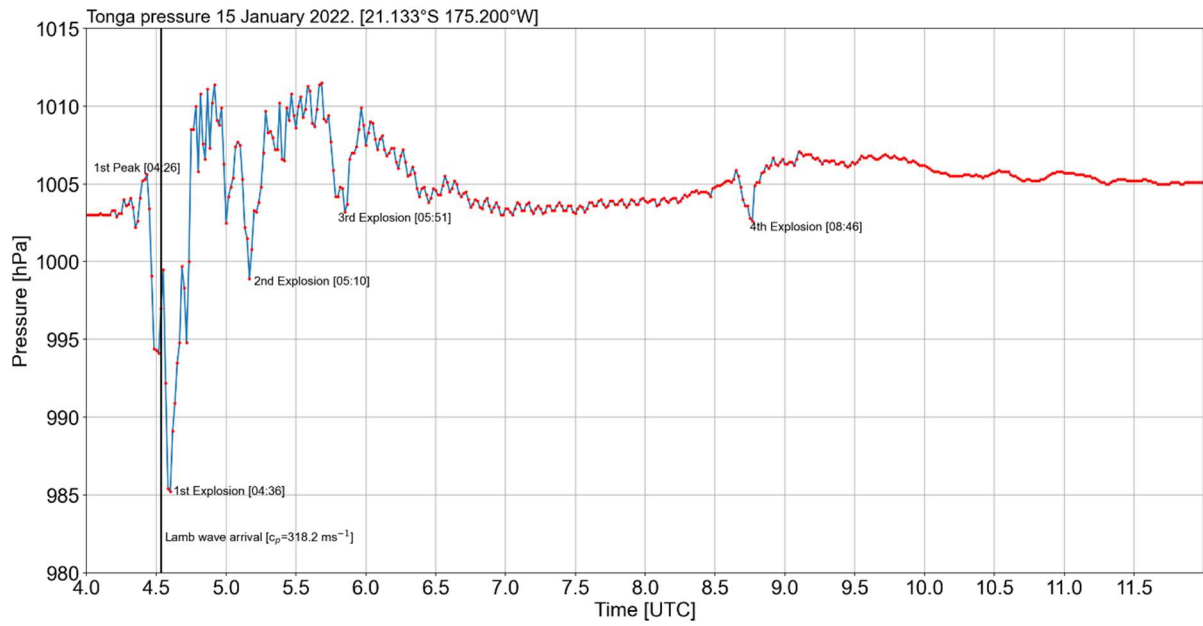
492 Extended Data Figure 5: 2D S-Transform³⁷ (2DST) estimates of gravity wave properties measured by AIRS in a descending-node pass over the Pacific Ocean on the 15th of January 2022. (top) temperature perturbations relative to a fourth-order polynomial fit across track. (middle) amplitudes estimated from these perturbations using the 2DST. (bottom) horizontal wavelengths estimated from these perturbations using the 2DST.



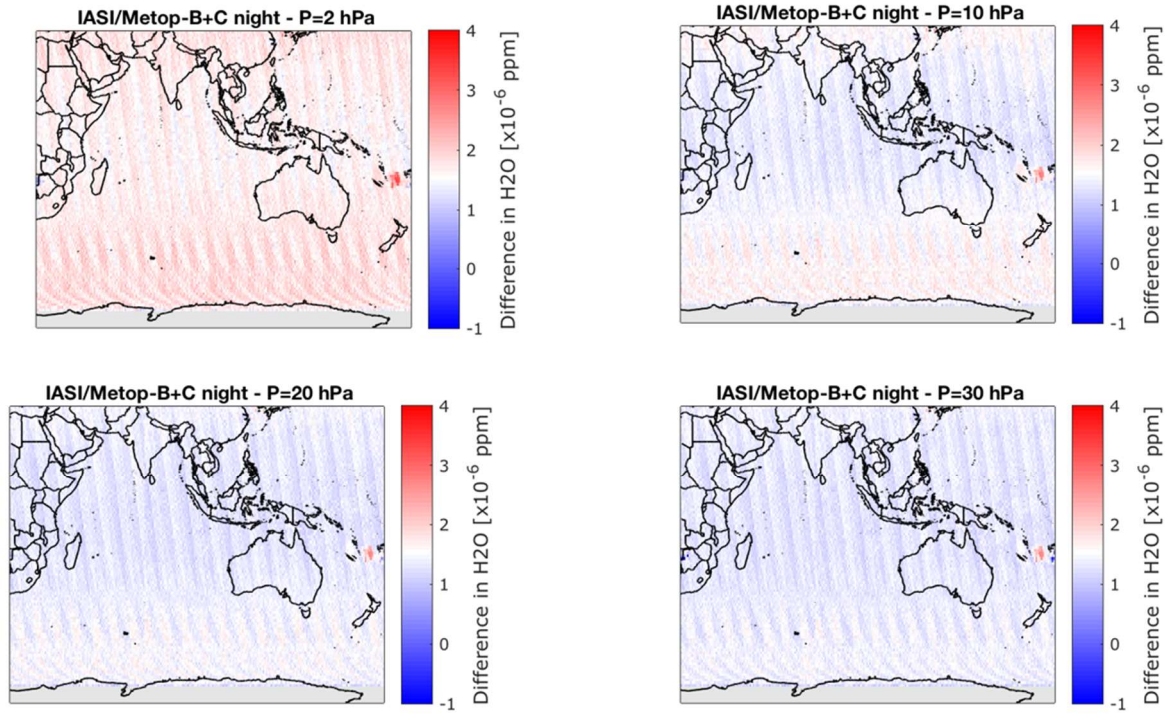
Extended Data Figure 6: Expected maximum speed of a gravity wave packet relative to the observed Lamb wave, as a function of horizontal gravity wave wavelength. Blue line thickness represents the range of Lamb wave propagation speeds that we compute from AIRS, with the fast edge being approximately equal to the speed of the surface pressure signal. Orange lines represent the fast limit of gravity wave phase speeds versus horizontal wavelength, which is in the limit that the vertical wavenumber $\rightarrow 0$. This has been calculated using the upper and lower Lamb wave speeds as the sound speed for this calculation, shown as two closely-overlaid orange lines.



Extended Data Figure 7: (a-c) transit of the leading gravity wave packet over the antipode in CrIS and AIRS 4.3 μm data (d-o) GW amplitudes over Pacific computed from AIRS, IASI and CrIS 4.3 μm data using the 2DST³⁷.



496 Extended Data Figure 8: Pressure measurements from 04:00 – 12:00 UTC from Tonga, ~64km from Hunga Tonga. Note the multiple explosions after the initial primary Lamb wave trigger.



Extended Data Figure 9: Excess of H₂O (difference between the observation and the zonal mean) measured by IASI-B and IASI-C over Tonga at 30, 20, 10 and 2 hPa.